Coexistence of Two Different Distorted Octahedral $[MnF_6]^{3-}$ Sites in $K_3[MnF_6]$: Manifestation in Spectroscopy and Magnetism

Christiane Stoll,[a] Mihail Atanasov,*[b, f] Jascha Bandemehr,[c] Frank Neese,*[b] Clemens Pietzonka,[c] Florian Kraus,[c] Antti J. Karttunen,[d] Markus Seibald,[e] Gunter Heymann,[a] and Hubert Huppertz*[a]

Dedicated to Prof. Dr. Dirk Reinen on the occasion of his 90th birthday

Abstract: As a consequence of the static Jahn-Teller effect of the ^5E ground state of Mn^{III} in cubic structures with octahedral parent geometries, their octahedral coordination spheres become distorted. In the case of six fluorido ligands, $[MnF_6]^{3-}$ anions with two longer and four shorter Mn–F bonds making elongated octahedra are usually observed. Herein, we report the synthesis of the compound $K_3[MnF_6]$ through a high-temperature approach and its crystallization by a high-pressure/high-temperature route. The main structural motifs are two quasi-isolated, octahedron-like $[MnF_6]^{3-}$ anions of quite different nature compared to that met in ideal octahedral Mn^{III} Jahn-Teller systems. Owing to the internal electric field of C_i symmetry dominated by the next-neighbour K^+ ions acting on the Mn^{III} sites, both sites, the pseudo-rhombic (site 1) and the pseudo-tetragonally elongated (site 2) $[MnF_6]^{3-}$ anions are present in $K_3[MnF_6]$. The compound was characterized by single-crystal and powder X-ray diffraction, and magnetometry as well as by FTIR, Raman, and ligand field spectroscopy. A theoretical interpretation of the electronic structure and molecular geometry of the two Mn sites in the lattice is given by using a vibronic coupling model with parameters adjusted from multireference ab-initio cluster calculations.

Introduction

Ternary hexafluoridomanganates have been well known since the middle of the 20th century. The oxidation state of manganese in these compounds has been mostly noted to be +IV, with $A_2[MnF_6]$ (A = Li, Na, K, Rb, Cs)[1] and $A'[MnF_6]$ (A' = Mg, Ca, Sr, Ba)[2] as the most common representatives. It is surprising that few reports refer to (pseudo)ternary hexafluoridomanganates(III), with $Na_3[MnF_6]$,[3,4] $K_3[MnF_6]$,[4–6] and $(NH_4)_3[MnF_6]$[5] as the better known compounds. As those compounds seem to exhibit quite complicated twinning as well as superstructures, $Na_3[MnF_6]$ is the only representative, where the crystal structure has been elucidated.[7] It crystallizes in space group $P12_1/n1$ (cryolite structure type) with the lattice parameters $a = 5.47$, $b = 5.68$, $c = 8.07$ Å, $\beta = 88.96°$, and a volume of $V = 251$ Å^3.[3] Before the description of $Na_3[MnF_6]$ by Massa and co-workers,[3] Ryss and Wituchnowskaja[5] reported the existence and syntheses of crimson colored $K_3[MnF_6]$ and $(NH_4)_3[MnF_6]$, the first representatives of (pseudo)ternary hexafluoridomanganates in oxidation state +III for the Mn atoms. Two years later, Peacock[6] described $K_3[MnF_6]$ as blueish-violet and determined the crystal system by X-ray photographs to be tetragonal with quite large

[a] Dr. C. Stoll, Assoc. Prof. Dr. G. Heymann, Prof. Dr. H. Huppertz
Universität Innsbruck
Institut für Allgemeine, Anorganische und Theoretische Chemie
Innrain 80–82, 6020 Innsbruck (Austria)
E-mail: Hubert.Huppertz@uibk.ac.at

[b] Prof. Dr. M. Atanasov, Prof. Dr. F. Neese
Max-Planck-Institut für Kohlenforschung
Kaiser-Wilhelm-Platz 1, 45470 Mülheim an der Ruhr (Germany)
E-mail: mihail.atanasov@kofo.mpg.de
frank.neese@kofo.mpg.de

[c] J. Bandemehr, C. Pietzonka, Prof. Dr. F. Kraus
Philipps-Universität Marburg,
Fachbereich Chemie, Anorganische Chemie, Fluorchemie
Hans-Meerwein-Straße 4, 35032 Marburg (Germany)

[d] Prof. Dr. A. J. Karttunen
Department of Chemistry and Materials Science
Aalto University, 00076 Aalto (Finland)

[e] Dr. M. Seibald
OSRAM Opto Semiconductors GmbH
Mittelstetter Weg 2
86830 Schwabmünchen (Germany)

[f] Prof. Dr. M. Atanasov
Institute of General and Inorganic Chemistry
Bulgarian Academy of Sciences
Akad. G. Bontchev Street, Bl.11, 1113 Sofia (Bulgaria)

Supporting information for this article is available on the WWW under https://doi.org/10.1002/chem.202005496

lattice parameters of $a = 17.50$, $c = 16.60$ Å, and a cell volume of $V = 636$ Å^3.[6]

As a detailed structural characterization of $K_3[MnF_6]$ was still missing, we synthesized the compound and determined its crystal structure. We analyzed the molecular geometry and electronic structure of the two differently distorted $[MnF_6]^{3-}$ sites and the consequences for the spectroscopic and magnetic behavior of the compound using correlated multireference electronic structure calculations, allowing one to make predictions for more detailed structural, magnetic, and spectroscopic studies.

Results and Discussion

The synthetic route of Peacock's initial preparation of $K_3[MnF_6]$ differs from the one we used here. He added $K_2MnF_5{\cdot}H_2O$ to molten KHF_2 at 400 °C,[6] whereas we synthesized the title compound from MnO_2 and KHF_2 at 800 °C in closed vessels or through a high-pressure/high-temperature experiment. Evidently Mn^{IV} is not stable under these conditions as $K_3[MnF_6]$ is formed. For details see the Experimental Section.

Crystal structure of $K_3[MnF_6]$ and molecular geometry of the $[MnF_6]^{3-}$ anions

The compound $K_3[MnF_6]$ crystallizes in the tetragonal space group $I4_1/a$ (no. 88) with the lattice parameters $a = 12.345(1)$, $c = 16.471(1)$ Å, and a volume of $V = 2510(2)$ Å^3 (selected crystallographic data is listed in Table 1). This is different than reported by Peacock. He observed a "pseudo-cell" with the lattice parameters of $a = 8.75$, $c = 8.30$ Å, and $V = 635$ Å^3 and gave a "true cell" of eight-fold volume with $a = 17.50$, $c = 16.60$ Å, and $V = 5083$ Å^3.[6] So, the cell volume of Peacock's "pseudo-cell" is approximately by a factor of four smaller, while the "true cell" is about twice the one observed by us. The "true" lattice parameter a determined by him is by a factor of approximately $\sqrt{2}$ larger than ours. Even though one could think that the lattice parameters in previous works have been assigned wrongly, we want to stress the point, that there is the possibility that $K_3[MnF_6]$ synthesized within this work represents a different modification of this substance than the one within Peacock's report, as the synthetic routes differ greatly. Such a slight variation of the lattice parameters between two different modifications is also observed in $KCuF_3$.[8–9]

The unit cell of $K_3[MnF_6]$ reported here contains 16 formula units comprising 160 atoms. The main motifs of the crystal structure are quasi-isolated $[MnF_6]^{3-}$ complex anions, with Mn···Mn distances of at least 6 Å. Two crystallographically different manganese positions Mn(1) and Mn(2) are present, both exhibiting distorted octahedral coordination spheres (Figure 1). The Mn(1) atom resides on Wyckoff position 8*d* ($\bar{1}$, C_i), and the Mn(2) atom occupies the 8*c* ($\bar{1}$, C_i) site. Table S1 and S2 in the Supporting Information contain the atomic coordinates, Wyckoff positions, and anisotropic displacement parameters.

Table 1. Selected crystallographic data and details of the structure determination of $K_3[MnF_6]$.

empirical formula	**$K_3[MnF_6]$**
molar mass [g mol^{-1}]	286.24
crystal system	tetragonal
space group	$I4_1/a$ (no. 88)
Powder data	
powder diffractometer	Stoe Stadi MP
radiation	$Cu_{K\alpha1}$ ($\lambda = 1.54060$ Å)
a [Å]	12.374(1)
c [Å]	16.575(1)
V [Å^3]	2537.7(1)
T [K]	293(2)
Single-crystal data	
single-crystal diffractometer	Bruker D8 Quest Photon 100
radiation	$Mo_{K\alpha}$ ($\lambda = 0.7107$ Å)
a [Å]	12.345(1)
c [Å]	16.471(1)
V [Å^3]	2510.0(2)
formula units per cell, Z	16
calculated density [g cm^{-3}]	3.03
T [K]	183(2)
absorption coefficient [mm^{-1}]	4.13
$F(000)$ [e]	2176
2θ range [°]	4.1-75.7
range in hkl	±21, ±21, ±28
total no. of reflections	101994
independent reflections / R_{int}	3394 / 0.0537
reflections with $I > 2\sigma(I)$	2877
data / ref. parameters	3394 / 95
goodness-of fit on F_o^2	1.099
absorption correction	semi-empirical (from equivalents)
final $R1/wR2$ ($I \geq 2\sigma(I)$)	0.0201 / 0.0361
final $R1/wR2$ (all data)	0.0295 / 0.0379
largest diff. peak/hole [e Å^{-3}]	0.46 / −0.46

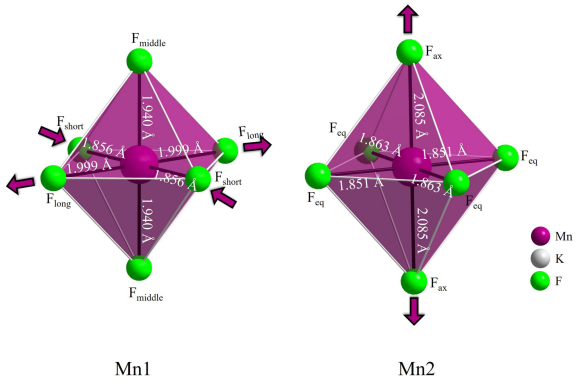

Figure 1. The two crystallographically different Mn atoms of $K_3[MnF_6]$ with distorted octahedral coordination spheres. The $[Mn(1)F_6]^{3-}$ anion is "pseudo-rhombic" (see text) and the symmetry is close to D_{2h}, while the $[Mn(2)F_6]^{3-}$ anion is "pseudo-tetragonal" with two (four) long (short) axial (equatorial) Mn–F bond lengths and close to D_{4h} symmetry. The numbering of the atoms is shown in Figure S1.

The Mn–F bond lengths vary between 1.856(1) and 2.086(1) Å (Table S3), which is in accordance with the bond lengths given in literature for the $[MnF_6]^{3-}$ anion in $Na_3[MnF_6]$ (1.897(1) to 2.018(1) Å) having in mind that vibronic effects within the cryolite-type structure are partly suppressed.[3] Within the recently discovered substance Na_3MnThF_{30}, the Jahn-Teller

effect seems to be suppressed leading to six equivalent bonds with the length of 1.937(2) Å.[10] This is in good accordance to the average Mn–F bond lengths within $K_3[MnF_6]$ (Mn(1)–F = 1.932 Å; Mn(2)–F = 1.933 Å). Interestingly, this is also the bond length value of an hypothetical undistorted octahedron, around which plasticity of the coordination sphere of Jahn-Teller active cations like Cu^{II}, as reported by Gazo et al., may work.[11] While the two *trans* Mn(1)–F bond lengths in axial positions, R_{medium} = 1.940(1) Å, exceed by only 0.008 Å the average octahedral Mn–F distance of 1.932 Å, the equatorial ones, R_{short} = 1.856 Å and R_{long} = 2.018 Å, display quite significant rhombic "splitting", −0.077 and 0.067 Å, respectively, away from the average octahedral distance. Having this in mind, hereafter we will refer to this site as "pseudo-rhombic". The other manganese atom Mn(2) shows a different structural distortion with the two Mn(2)–F_{ax} bond lengths elongated to 2.086(1) Å in comparison to the four Mn(2)–F_{eq} bond lengths of 1.851(1) and 1.863(3) Å.

The surrounding of the two different $[MnF_6]^{3-}$ anions by potassium cations also differs from each other. In total, the $[Mn(1)F_6]^{3-}$ anion is surrounded by 14 K^+ ions. All but two edges (Figure 2, left, marked blue) of the rhombically distorted $[Mn(1)F_6]^{3-}$ octahedron are bridged in a μ_2-manner by ten K^+ ions (Figure 2, left, light gray), while the other four K^+ ions (Figure 2, left, dark gray) are bound to its corners. A closer look at F_{short} shows a coordination of three potassium cations with K–F bond lengths in the range of 2.699(1) to 2.842(1) Å and one potassium cation coordination with a quite large K–F bond length of 3.168(1) Å (Figure 2, left, dashed yellow line). Therefore, the coordination around $F(3)_{short}$ can be described as 3 + 1, which would in turn open up two of the μ_2-bridges above two of the edges of the distorted octahedra (Figure 2, left, marked solid yellow). The displayed arrangement of the 14 potassium cations forming a distorted tetrakis-hexahedron around the $[Mn(1)F_6]^{3-}$ anion (Figure 2, left) leads to a pseudo-rhombically distorted octahedral fluorine coordination of Mn(1).

The $[Mn(2)F_6]^{3-}$ anion is also surrounded by 14 K^+ ions, but in this case all eight faces of the elongated $[Mn(2)F_6]^{3-}$ octahedron are μ_3-capped by K^+ cations and the residual six K^+ ions are bound to its corners. The Mn(2) atom is thus surrounded by six F^- anions in the first ligand shell, cube-shaped by K^+ atoms in the second shell (Figure 2, right, dark gray), and again octahedrally by K^+ atoms in the third shell (Figure 2, right, light gray), leading to a rhombic dodecahedron (Figure 2, right) of K^+ ions. The latter six potassium atoms however belong to the twofold-capped hexagonal prisms around $[Mn(2)F_6]^{3-}$. All F atoms of the $[Mn(2)F_6]^{3-}$ anion are coordinated by five K^+ atoms. This leads to an elongated octahedral geometry for the $[Mn(2)F_6]^{3-}$ anion, as the F_{ax} atoms are pulled outwards in a linear manner ($\angle_{Mn(2)\text{-}Fax\text{-}K1}$ = 177.7(1)°) by the potassium cations K(1). In contrast, the potassium cations pulling outwards in equatorial positions show Mn–F–K1 angles of 166.2(1) and 167.2(1)° for Mn(2)–$F(4)_{eq}$–K1 and Mn(2)–$F(1)_{eq}$–K1, respectively. Compared to the geometric distortion leading to pseudo-rhombic $[Mn(1)F_6]^{3-}$ anions, where no or less interaction of potassium cations with the tips of the octahedron (F_{ax}) seems to be present, a geometric distortion is observed

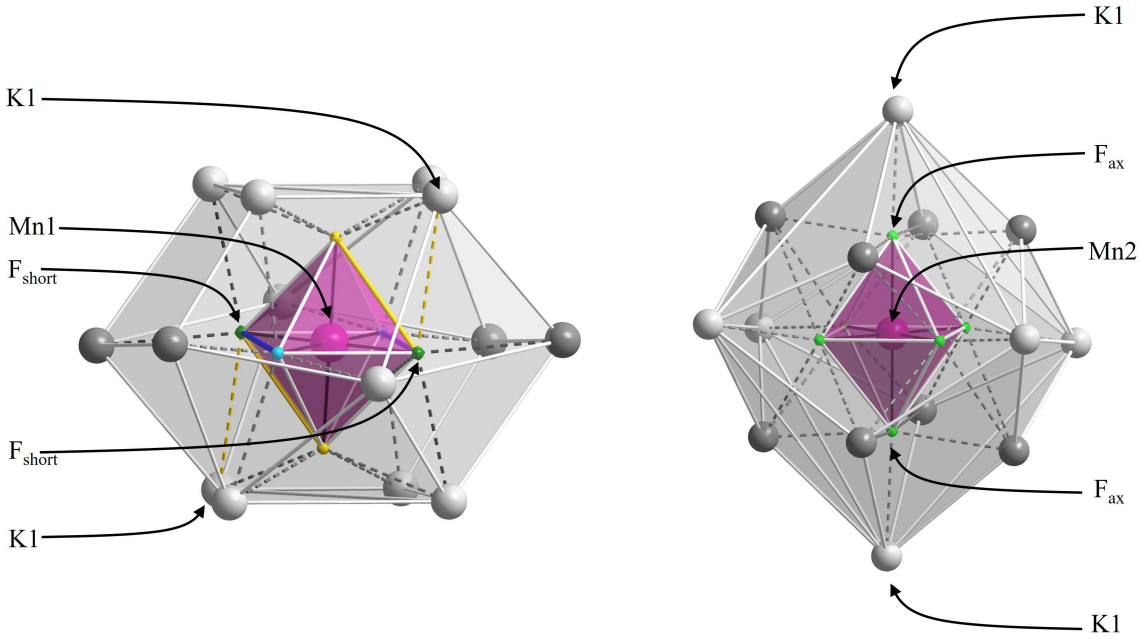

Figure 2. Left: Distorted tetrakis-hexahedral coordination sphere of the pseudo-rhombically distorted $[Mn(1)F_6]^{3-}$ octahedron. The F_{short}, F_{medium}, and F_{long} sites are marked dark green, yellow, and light blue, respectively. The long bond between F_{short} and K1 is indicated by a dashed, yellow colored line, signaling the 3 + 1 coordination of F_{short}, which leads to the opening of the bridge at the yellow marked edges. Blue edges of the pseudo-rhombically distorted octahedra mark the two edges that are not bridged in a μ_2-manner by K^+ cations. Potassium cations in a darker shade of gray represent the cations that are just bound to one corner of the $[Mn(1)F_6]^{3-}$ anion. Right: Twofold-capped hexagonal prismatic coordination sphere of the elongated $[Mn(2)F_6]^{3-}$ octahedron. Here, the potassium cations of the second shell (cuboid) are drawn in a slightly darker gray than the ones of the third shell (octahedron). F atoms are pictured in green, Mn atoms in purple, and K atoms in gray. Detailed numbering of the atoms is given in Figure S2.

that leads to the elongation of the $[Mn(2)F_6]^{3-}$ anion, typical for Jahn-Teller ions in d^4 high-spin ground states. Additionally, the $[MnF_6]^{3-}$ units are embedded in a matrix of potassium cations (five crystallographically different cations), which all show individual coordination spheres. K1 and K4 are eightfold coordinated, K2 ninefold, K3 tenfold, and K5 twelvefold by fluorine atoms with bond distances varying from 2.537(1) to 3.233(1) Å (Table S3).

After this local structure description, we come to a topological description of the crystal structure. Within the crystal structure, the Mn atoms form 4.4.4.4 square nets parallel to the *ab*-plane. These planes are stacked in an AB-like manner, thus similar to the atom arrangement within the crystal structure of tungsten. Here, the two different kinds of quasi-isolated $[MnF_6]^{3-}$ distorted octahedra are arranged alternatingly in lines along the crystallographic *a*- and *b*-axes.

The structure shows similar features to the sodium analog $Na_3[MnF_6]$, which adopts the cryolite structure type.[3] A comparison of the crystal structures (Figure 3) shows that both structures contain quasi-isolated $[MnF_6]^{3-}$ distorted octahedra, although differently arranged. Within $Na_3[MnF_6]$, the arrangement is ferrodistortive (elongated axes of distorted octahedra are parallel), whereas in $K_3[MnF_6]$ it is not. Other differences between the crystal structures are the size of the unit cells, of which $K_3[MnF_6]$ exhibits an approximately eight times larger volume than $Na_3[MnF_6]$, and the positions of the alkali metal cations.

To check the reliability of the crystal structure model, bond-length/bond-strength (BLBS),[12,13] CHARDI,[14] and MAPLE[15–17] calculations were conducted, which are in good agreement with the crystal structure. These results are shown in the Tables S5 and S6.

The crystal structure could also be verified by a Rietveld analysis of the powdered sample of $K_3[MnF_6]$, shown in Figure 4 (the sample was synthesized by Hofmann in the late 1970s[18]). The composition of this sample could be determined to 98.8(1) wt% $K_3[MnF_6]$ and 1.2 wt% $KMnF_3$ by weight. Further details on the Rietveld refinement are listed in Table S7. A comparison of the Mn–F bond lengths resulting from the Rietveld refinement with the Mn–F bond-lengths resulting from the single-crystal analysis is shown in Table S8. It is obvious that the structural model, showing a pseudo-rhombic and a pseudo-tetragonal elongated octahedral unit could be confirmed by the Rietveld refinement.

Additionally, FTIR (Figure S3) and Raman (Figure S4) spectra confirm the presence of $[MnF_6]^{3-}$ units as well as the absence of O–H bonds.

Magnetic studies

Direct current (DC) magnetic data, temperature- and field-dependent, of $K_3[MnF_6]$ were recorded with the vibrating sample magnetometer (VSM) option of a physical property measurement system (ppms). The temperature dependent scans from 1.8 to 300 K were taken with applied fields from −9 to 9 T in steps of 1 T. The collected data were corrected with respect to the diamagnetic moment of the sample holder, as well as to the diamagnetic contribution ($\chi_{dia} = -1.22 \cdot 10^{-4}\ cm^3\,mol^{-1}$) of the sample derived from Pascal constants. The result is the net paramagnetic data. As can be seen from the χT versus T plot (Figure 5), the sample behaves like a Curie-like paramagnet with room temperature values close to the one ($\chi T = 0.5S(S+1) = 3$) expected for a $S = 2$ spin. The χT versus T plot with data from CASSCF/NEVPT2 multi-reference electronic calculations utilizing the X-ray geometries of the $[Mn(1)F_6]^{3-}$ and $[Mn(2)F_6]^{3-}$ polyhedra are close to each other, and for ranges of temperatures between 100 and 300 K coinciding with the measured values. The deviations between measurement and theoretical calculations signal that some weak dipolar interactions (not taken into account in the molecular ab-initio calculations) and (or) that impurities (vide supra) are present.

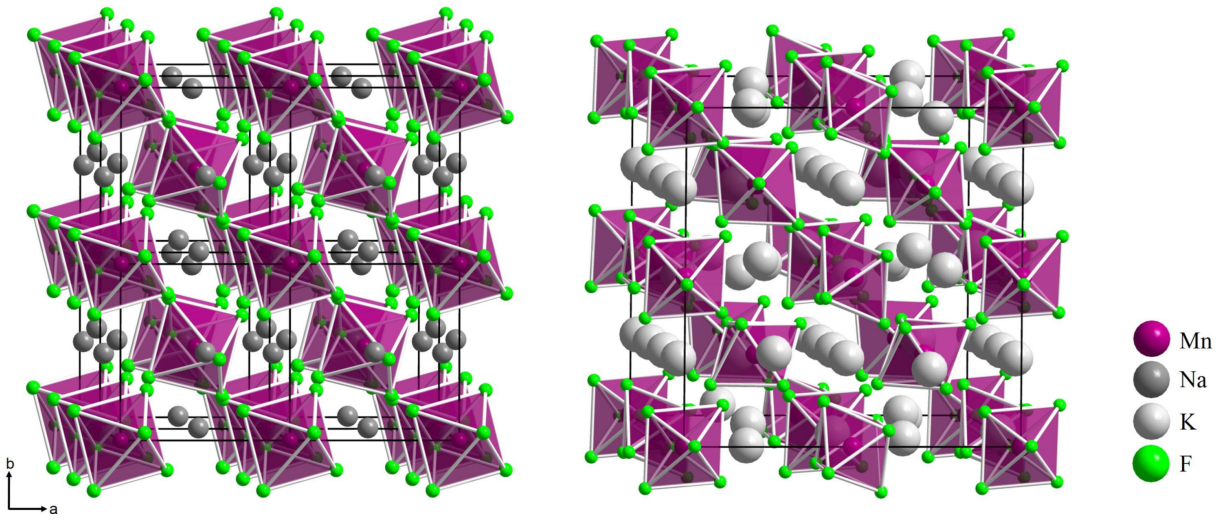

Figure 3. Comparison of the crystal structures of $Na_3[MnF_6]$ (cryolite structure type, left) and $K_3[MnF_6]$ (right).

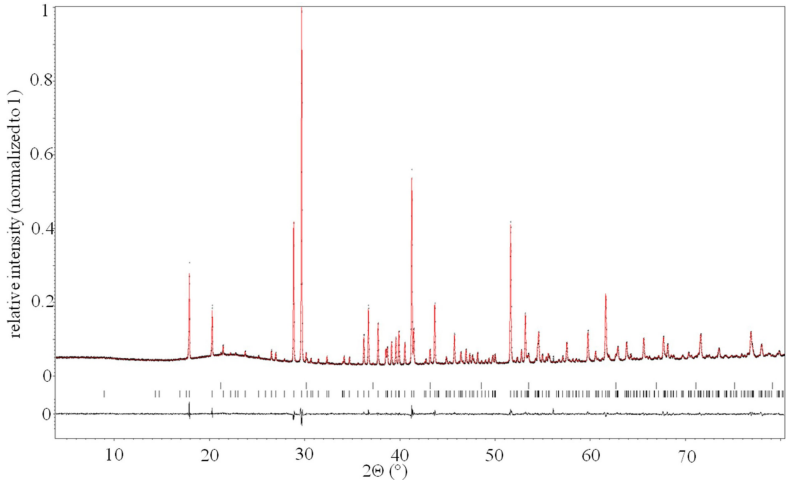

Figure 4. Observed (black) and calculated (red) X-ray powder pattern of $K_3[MnF_6]$ with a small amount of $KMnF_3$ (1.2 wt%) after Rietveld refinement. The calculated reflection positions are indicated by vertical bars below the patterns (top: $KMnF_3$, bottom: $K_3[MnF_6]$). The curve at the bottom represents the difference between the observed and the calculated intensities. $R_p = 11.84$, $R_{wp} = 8.90$, $S = 1.64$.

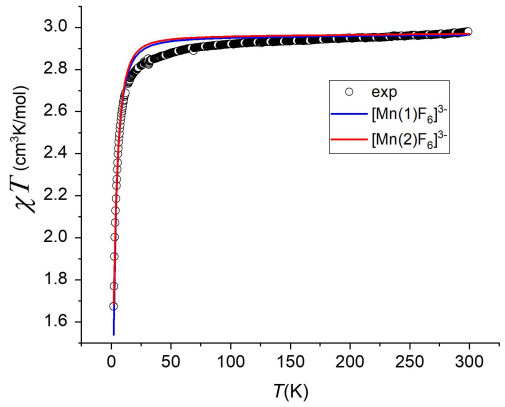

Figure 5. χT versus T plot recorded at a field of $B = 1$ T (○) and from correlated CASSCF/NEVPT2 calculations using the X-ray geometries for the pseudo-rhombic (——) and pseudo-tetragonal (——) $[MnF_6]^{3-}$ magnetic centers.

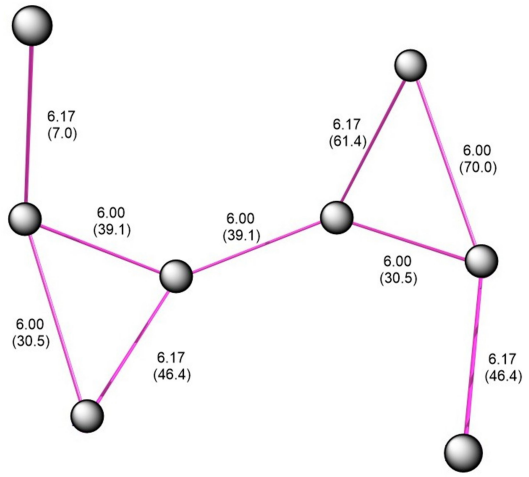

Figure 6. Topology of the closest contacts within the magnetically inequivalent Mn(1) subset of pseudo-rhombic $[MnF_6]^{3-}$ site; closest Mn···Mn interatomic distances [Å] and relative orientation of short axes of pairs [°].

Field dependent data were recorded between 1.8 and 300 K in zero-field-cooled and field-cooled modus at magnetic field values of $B = 1$ to 9 T in steps of 1 T. The coincidence of the field and zero-field cooled magnetizations shows no hysteresis opening, as expected due to the large Mn···Mn distances and correspondingly weak dipolar interactions between closest Mn neighbors (Figures 6 and 7) and relatively small zero-field splitting for the sites Mn(1) and Mn(2) (see Theoretical Section).

In Figure 8, the iso-field values of the magnetizations in the temperature range from 2 to 15 K at fields $B = 1$, 5, and 9 T are plotted. The *nesting* of the low-temperature iso-field values of the magnetization and their deviations from the Brillouin function plot for an isotropic $S = 2$ spin (Figure 8, broken line) reflects a small yet important (see below) magnetic anisotropy. This behavior will be subject to a theoretical analysis below.

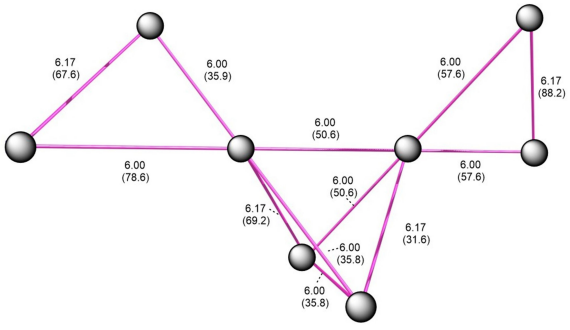

Figure 7. Topology of the closest contacts within the magnetically non-equivalent Mn(2) subset of the pseudo-tetragonal $[MnF_6]^{3-}$ elongated octahedra; closest Mn–Mn interatomic distances [Å] and relative orientation of long axes of pairs [°].

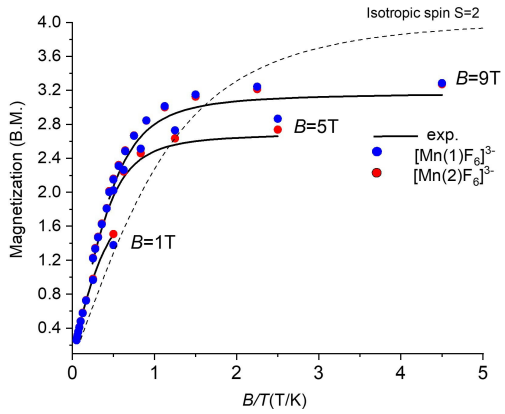

Figure 8. Plot of iso-field values of the magnetization versus the reduced parameter B/T from experiment (——) and from CASSCF/NEVPT2 multi-reference electronic structure calculations using the X-ray geometry for the pseudo-rhombic (•) and the pseudo-tetragonal elongated octahedra (•). Broken lines show the magnetization according to the expression $M = N_A g S \mu_B B_S(y)$; $y = g\mu_B SB/k_B T$ in terms of the Brillouin function describing a hypothetical isotropic $S = 2$ spin.

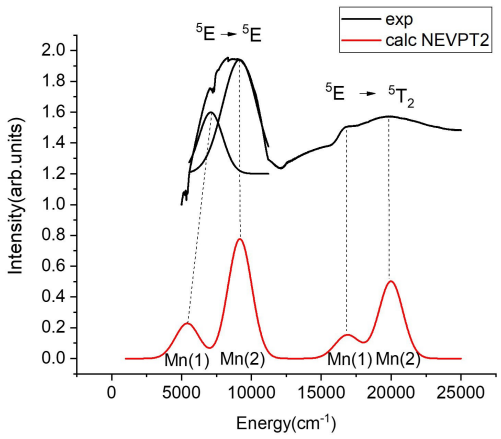

Figure 9. Experimental (——) and theoretical [CASSCF(NEVPT2)] (——) spectra originating from the pseudo-rhombic $[Mn(1)F_6]^{3-}$ and pseudo-tetragonal elongated $[Mn(2)F_6]^{3-}$ anions in $K_3[MnF_6]$ of this work; the theoretical spectra were computed by imposing an off-centric distortion on four in-plane F atoms of the two Mn sites, consisting of a shift of the z coordinate of these ligands by 0.1 Å.

d–d absorption spectra

The electronic excitation spectrum of a powder of $K_3[MnF_6]$ prepared by Peacock's method,[6] recorded using diffuse reflection, was communicated by Hatfield and Parker.[19] They report two d-d bands at 9000 and 18000 cm^{-1}. Such spectral pattern is typical for Jahn-Teller distorted high-spin pseudo-octahedral complexes of Mn^{III}.[20] The 9000 cm^{-1} band was assigned to the electronic transition from the lower to the upper split components of the ^5E_g octahedral parent term of the Mn^{III} atom, in this case to the $^5B_{1g} \rightarrow {}^5A_{1g}$ transition within tetragonally elongated $[MnF_6]^{3-}$ octahedra (term notations in their interpretations refer to the D_{4h} point groups). The second transition at 18000 cm^{-1} was assigned to a transition from the $^5B_{1g}$ ground state into the $^5T_2$ (O_h) split (but not resolved) electronic sublevels of tetragonally elongated $[MnF_6]^{3-}$ octahedra. In the structure of $K_3[MnF_6]$ reported here, the presence of the two $[MnF_6]^{3-}$ complex anions with quite different molecular geometries and electronic structures leads one to expect two sets of such transitions. These are indeed present in the spectrum of $K_3[MnF_6]$ (Figure 9): The one due to the $^5A_g(1)(^5E_g) \rightarrow {}^5A_g(3)$, $^5A_g(4)$, $^5A_g(5)(^5T_{2g})$ (symmetry notations using $C_i(O_h)$ point group symmetries) shows up very clearly and directly at 16800 and 19800 cm^{-1}, whereas the band centered at 9000 cm^{-1} shows this indirectly, reflected by its asymmetric shape with a less intense shoulder at low energy and a more intense maximum at higher energy. A deconvolution of this band into two Gauss curves allows to identify the $^4A_g(1) \rightarrow {}^4A_g(2)(C_i)$ transitions within the ^5E_g (O_h) components for the two sites at 7000 and 9000 cm^{-1} (symmetry notations pertain to $C_i(O_h)$ point group symmetries).

The reported four observed d-d transitions are nicely reproduced from CASSCF/NEVPT2 cluster calculations computed using the X-ray structures of the $[Mn(1)F_6]^{3-}$ and $[Mn(2)F_6]^{3-}$ anions and allowing for a tiny distortion along a $\tau_{2u}(O_h)$ type normal mode. Such off-centric distortions are the source of intensity of complexes having a center of inversion, where d-d transitions are formally forbidden by the Laporte rule. Because of the larger vibronic stabilization energy in the case of the tetragonally elongated structure compared to the pseudo-rhombic one (see analysis below), *both* the splitting of the ^5E_g parent octahedral ground state, as well as the energy separation from the $^5T_2$ excited states are larger for the pseudo-tetragonal Mn(2) site, than for the pseudo-rhombic Mn(1) site. In the approximation of a D_{4h} symmetry (Mn(2) site) (the real symmetry is C_i, see below), this leads to an assignment of the bands at 9200 and 19800 cm^{-1} to the $^5B_{1g}(^5E_g) \rightarrow {}^5A_{1g}(^5E_g)$ and $^5B_{1g}(^5E_g) \rightarrow {}^5B_{2g}$, $^5E_g(^5T_{2g})$ transitions for the pseudo-tetragonal elongated complex $[Mn(2)F_6]^{3-}$, respectively, while the corresponding red shifted transitions at 7000 and 16800 cm^{-1} are assigned to the $^5A_g(1)(^5E_g) \rightarrow {}^5A_g(2)(^5E_g)$ and $^5A_g(1)(^5E_g) \rightarrow {}^5A_g(3)$, $^5A_g(4)$, $^5A_g(5)(^5T_{2g})$ transitions for the pseudo-rhombic complex $[Mn(1)F_6]^{3-}$, respectively ($C_i(O_h)$ term notations).

Theoretical Calculations and Analysis

Chemical bonding in the pseudo-tetragonal and pseudo-rhombic $[MnF_6]^{3-}$ anions

Computations using the X-ray geometries of the $[Mn(2)F_6]^{3-}$ and $[Mn(1)F_6]^{3-}$ anions in $K_3[MnF_6]$ allow to extract a ligand field 3*d*-MO energy diagram and to plot orbital shapes in the two complexes depicted in Figure 10.

The energy diagrams for the two sites differ in the nature of the highest singly occupied MO; being d_{z^2} type for $[Mn(2)F_6]^{3-}$ and an almost equal mixture of $d_{x^2-y^2}$ and d_{z^2} in the case of $[Mn(1)F_6]^{3-}$. It also shows, in agreement with the X-ray geometries, that the orbital pattern for $[Mn(2)F_6]^{3-}$ anion is closer to a tetragonal geometry, while that for $[Mn(1)F_6]^{3-}$ anion reflects

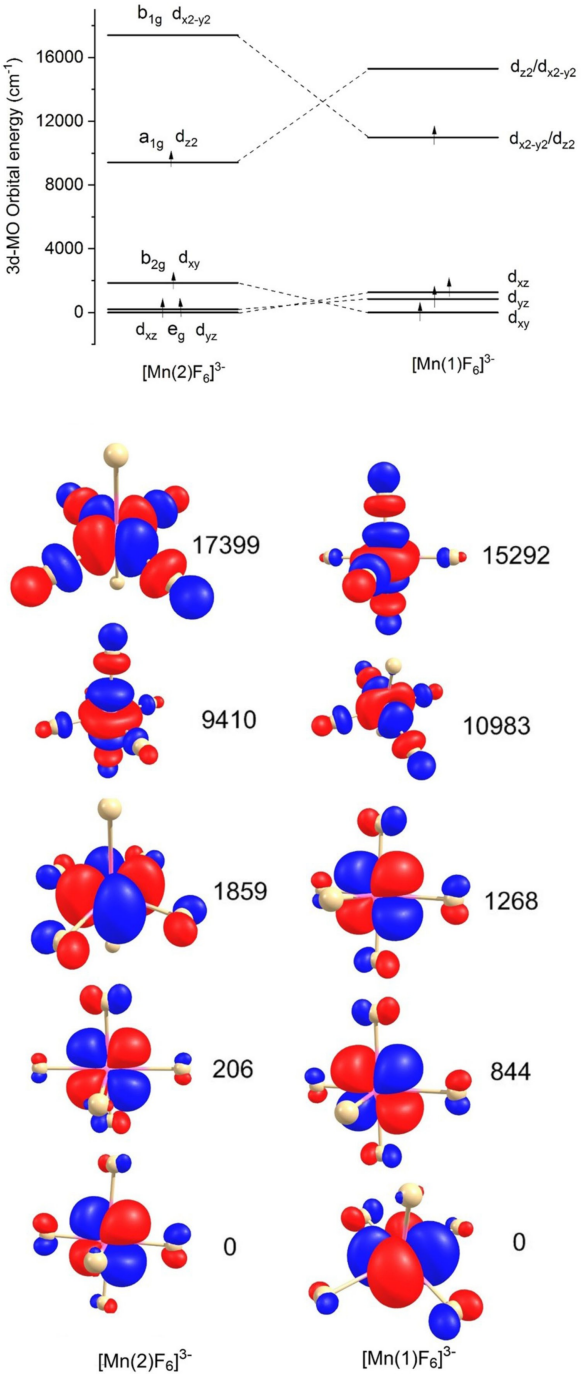

Figure 10. 3d-orbital energies obtained from ab-initio ligand field calculations for the pseudo-tetragonal elongated $[Mn(2)F_6]^{3-}$ and pseudo-rhombic $[Mn(1)F_6]^{3-}$ anions with X-ray geometries. Left: 3d-orbital ordering, notations follow the irreducible representations of the D_{4h} point group for $[Mn(2)F_6]^{3-}$; the MO symmetries of both sides in the real C_i point group of both ions are a_g. 3d-orbital contour diagrams were plotted by using contour values of the electron density 0.03 electron/bohr^3. Values of the parameters of interelectronic repulsion *B*, C(NEVPT2), and the spin-orbit coupling constants (CASSCF) obtained from the ab-initio ligand field theory (AILFT) are, respectively, 994, 3584, 343 cm^{-1} for the $[Mn(1)F_6]^{3-}$ anion and 999, 3570, 343 cm^{-1} for the $[Mn(2)F_6]^{3-}$ anion.

a net rhombicity as seen in the splitting of the d_{xz} and d_{yz} orbitals and the composition of the highest occupied MOs. This splitting reflects the off-axial C_i symmetry, which is much larger for $[Mn(1)F_6]^{3-}$ than for $[Mn(2)F_6]^{3-}$.

Orbital energy expressions given by the angular overlap model (AOM) for the $[Mn(2)F_6]^{3-}$ Equation (1) allow to rationalize the orbital levels scheme in terms of σ and π Mn–F interactions and to quantify these in terms of the e_σ and e_π parameters; the same equations are also valid for the pseudo-rhombic $[Mn(1)F_6]^{3-}$ site, except of having in addition an off-diagonal term accounting for $d_{z^2}/d_{x^2-y^2}$ mixing in the two highest 3d MOs.

$$\begin{aligned} e(d_{xz}) &= 2e_\pi^x + 2e_\pi^z \\ e(d_{yz}) &= 2e_\pi^y + 2e_\pi^z \\ e(d_{xy}) &= 2e_\pi^x + 2e_\pi^y \\ e(d_{z2}) &= 2e_\sigma^z + (1/2)(e_\sigma^x + e_\sigma^y) \\ e(d_{x2-y2}) &= (3/2)(e_\sigma^x + e_\sigma^y) \end{aligned} \quad (1)$$

With three different types of ligands on the *x*-, *y*-, and *z*-axes (neglecting small deviations of the ligands from these axes) there are three such sets of parameters. The following values have been deduced by taking a $1/R^n$ dependence of e_σ and e_π pertaining to an (hypothetical) undistorted octahedral $[MnF_6]^{3-}$ anion (see Supporting Information for a detailed description how their values are extracted), R(Mn–F) 1.933 Å: $e_\sigma = 6255$, $e_\pi = 1630$ cm^{-1}, and $n = 5.2$ for $[Mn(1)F_6]^{3-}$, and $e_\sigma = 5520$, $e_\pi = 1222$ cm^{-1}, and $n = 6.7$ for $[Mn(2)F_6]^{3-}$. The values of *n* are in the range of data reported on the pressure dependence of energies of d-d transitions of octahedral 3d complexes.[21] The parameters e_σ and e_π are also close to the ones extracted from the interpretation of d-d transitions of hexacoordinated complexes of Cr^{III} atoms with $e_\sigma = 7400$ and $e_\pi = 1700$ cm^{-1}.[22] From the values of e_σ and e_π and the relation $\Delta = 10Dq = 3e_\alpha - 4e_\pi$, we deduce the values $10Dq = 12\,245$ cm^{-1} for $[Mn(1)F_6]^{3-}$ and 11 670 cm^{-1} for $[Mn(2)F_6]^{3-}$ for the corresponding hypothetical octahedral $[MnF_6]^{3-}$ complexes. Angular overlap model parameters e_σ for the $[Mn(1)F_6]^{3-}$ and $[Mn(2)F_6]^{3-}$ compare well with data on $[MnF_6]^{3-}$ from literature.[20]

d-d transitions

The MO 3d energy ordering allows to rationalize and assign the ligand field transitions (Figure 9). Table 2 lists the calculated (NEVPT2) energies of d-d transitions for the two different Mn sites (cf. with the plotted theoretical spectrum of Figure 9).

d-d transitions in centrosymmetric complexes are forbidden by the Laporte selection rule but become allowed by instantaneous dynamic distortions along vibrational normal modes, which remove the center of inversion. For octahedral $[MnF_6]^{3-}$ anions these are the τ_{1u} (there are two such vibrations) and τ_{2u} normal modes. Table 3 lists the vibrational normal modes of the $[Mn(1)F_6]^{3-}$ and $[Mn(2)F_6]^{3-}$ coordination units. They have been computed based on DFT pre-optimized $[MnF_6]^{3-}$ geometries taking the geometries of the X-ray structures as starting ones (see Section IV.8 for computational details). From the normal

modes lacking a center of inversion, the τ_{2u} vibrations are most efficient in governing the d-d transition intensity. Their effect is due to a lowering of symmetry from D_{4h} to D_{2d} and were utilized in computing the spectral shape due to d-d transitions in Figure 9 (red solid lines); the agreement between computed and experimental spectral shapes is reasonable.

Magnetic anisotropy

Computed energy spectra allow to quantify and rationalize the low temperature dependence of the magnetic properties - the magnetic susceptibility and the magnetizations, in particular the magnetic anisotropy as reflected by the nesting of the iso-field lines of the reduced magnetizations. These anisotropies are governed by the spin-sublevels stemming from the spin-orbit splitting of the ^5A_g (C_i) ground states of the pseudo-rhombic ($[Mn(1)F_6]^{3-}$) and the pseudo-tetragonal ($[Mn(2)F_6]^{3-}$) anions, respectively. This behavior is described by the phenomenological spin Hamiltonian $\hat{H}_S$, with spin-operators $\hat{S}_x$, $\hat{S}_y$ and $\hat{S}_z$, acting on the spin $S=2$ basis functions ($M_s=0$, ±1, and ±2). μ_B is the Bohr magneton.

$$\hat{H}_S = D\hat{S}_z^2 + E(\hat{S}_x^2 - \hat{S}_y^2) + \mu_B(g_x\hat{S}_xB_x + g_y\hat{S}_yB_y + g_z\hat{S}_zB_z) \quad (2.1)$$

The D and E terms describe the axial and orthorhombic zero-field splitting (ZFS); the third one is the Zeeman operator, describing the effect of the external magnetic field with the components B_x, B_y, and B_z along the axes for which the ZFS and the Zeeman term are diagonal. The ZFS parameters D and E are related with the parameters D_{zz}, D_{xx}, and D_{yy}, the traceless eigenvalues of the ZFS tensor, with the magnetic anisotropy axes x, y, and z:

$$D = (3/2)D_{zz} \quad (2.2)$$

$$E = (1/2)(D_{xx} - D_{yy}) \quad (2.3)$$

ZFS parameters and the g_x, g_y, g_z factors from ab-initio NEVPT2 calculations are listed in Table 4.

Whereas the g-factors show modest deviations from the free ion value, D and E reflect significant magnetic anisotropies. D is negative for the pseudo-tetragonal $[Mn(2)F_6]^{3-}$ but positive for the pseudo-rhombic $[Mn(1)F_6]^{3-}$ magnetic centers, implying that in the ground state the respective magnetic sublevels $M_s=\pm2$ and $M_s=0$, respectively are lowest in energy. The magnetic field along z leads to a first order splitting of the $M_s=\pm2$ pair, while leaving the $M_s=0$ state in the case of $[Mn(1)F_6]^{3-}$ to a first

Table 2. Energies [cm^{-1}] of d-d transitions for the pseudo-rhombic $[Mn(1)F_6]^{3-}$ and the pseudo-tetragonal $[Mn(2)F_6]^{3-}$ complexes in $K_3[MnF_6]$.[a]

$[Mn(1)F_6]^{3-}$		$[Mn(2)F_6]^{3-}$	
$\Delta_{z^2/x^2-y^2\rightarrow x^2-y^2/z^2}$	5280	$\Delta_{x^2-y^2\rightarrow z^2}$	9499
$\Delta_{z^2/x^2-y^2\rightarrow xz}$	17050	$\Delta_{x^2-y^2\rightarrow xy}$	18543
$\Delta_{z^2/x^2-y^2\rightarrow yz}$	17569	$\Delta_{x^2-y^2\rightarrow yz}$	20469
$\Delta_{z^2/x^2-y^2\rightarrow xy}$	18627	$\Delta_{x^2-y^2\rightarrow xz}$	20709

[a] To a good approximation, spin-allowed transitions for high-spin d^4 complexes do not depend on interelectronic repulsion. Therefore, d-d transitions are designated by the excitation of the single hole in the top most virtual d-MOs of the ^5A_g ground states of the $[Mn(1)F_6]^{3-}$ and $[Mn(2)F_6]^{3-}$ anions into the singly occupied 3d-MOs at lower energy (cf. Figure 9).

Table 3. Vibrations [cm^{-1}] in hypothetical elongated and compressed $[MnF_6]^{3-}$ and related anions from DFT geometry optimizations and Hessian calculations.

Vibration[a]	O_h	D_{4h}	$[MnF_6]^{3-}$ Compressed	$[MnF_6]^{3-}$ Elongated	$[ScF_6]^{3-}$	$[GaF_6]^{3-}$	$[VF_6]^{3-}$
ν_1	α_{1g}	α_{1g}	485	489	504	535	533
ν_2	ε_g	β_{1g}	-236	294	–	–	–
		α_{1g}	331	282			
ν_3	τ_{1u}	α_{2u}	263	300	–	298	292
		ε_u	260	292			
ν_4	τ_{1u}	α_{2u}	552	356	–	481	511
		ε_u	351	538			
ν_5	τ_{2g}	β_{2g}	238	291	370	281	–
		ε_g	264	243			
ν_6	τ_{2u}	β_{2u}	166	216	–	–	–
		ε_u	186	180			

[a] Labeling of octahedral vibrations follows notations by Nakamoto.[23] Vibrational frequencies for the regular octahedral $[ScF_6]^{3-}$(d^0), $[GaF_6]^{3-}$(d^{10}), and $[VF_6]^{3-}$(d^3) complexes are taken from the same monograph (see references cited therein).

Table 4. Magnetic parameters for Mn(1) and Mn(2) from NEVPT2 ab-initio calculations.[a]

	$D_{xx}(R_x)$	$D_{yy}(R_y)$	$D_{zz}(R_z)$	D	E	g_x	g_y	g_z
Mn(1)	−0.44(1.940)	−2.61(1.999)	3.05(1.856)	4.57	1.09	1.982	1.969	2.000
Mn(2)	1.32(1.863)	1.59(1.851)	−2.91(2.086)	−4.36	0.13	1.994	1.995	1.969

[a] Mn–F bond lengths correlating with the magnetic axes [Å] are listed in parenthesis for each main (canonical) D-tensor direction x, y, and z.

approximation unchanged. Magnetic fields along the *x* and *y* directions mix the ground states $M_s = \pm 2$ for $[Mn(2)F_6]^{3-}$ and $M_s = 0$, for $[Mn(1)F_6]^{3-}$ with $M_s = \pm 1$. Thus transversal (*x*, *y*) magnetic fields lower the magnetization for $[Mn(2)F_6]^{3-}$ and increase it for $[Mn(1)F_6]^{3-}$. This effect becomes increasingly pronounced upon increasing the external field or decreasing the temperature. This is nicely reflected by the iso-field lines of the magnetization (Figure 8).

Coexistence of the pseudo-rhombic $[Mn(1)F_6]^{3-}$ and the tetragonally elongated $[Mn(2)F_6]^{3-}$ anions in K_3MnF_6: Vibronic coupling analysis

Jahn-Teller effect in free hydrated $[MnF_6]^{3-}$

The ^5E_g ground state of octahedral $[MnF_6]^{3-}$ undergoes Jahn-Teller distortions along the ε_g vibrations (normal modes) with shapes as depicted in Figure 11.

The Q_θ normal coordinate distorts the octahedral $[MnF_6]^{3-}$ anion towards an elongated ($Q_\theta > 0$) or compressed ($Q_\theta < 0$) configuration with axial D_{4h} symmetry, while Q_ε lowers the symmetry to D_{2h}. The dependence of the ground state potential energy surface on the Q_θ and Q_ε normal coordinates is shown in the top of Figure 12. It has been derived using the theory of the Jahn-Teller effect[24] and model parameters adjusted from NEVPT2 calculations. In these calculations, we utilized DFT optimized geometries, which yield Mn–F bond lengths for the compressed and elongated D_{4h} structures listed in Table 5 (for details of the derivation see the Supporting Information). The potential surface shows energy minima for $[MnF_6]^{3-}$ anions in tetragonally elongated geometries with long Mn–F axes along the *z*, *x*, and *y* Cartesian axes. Taking a cross section of the potential surface along Q_θ ($Q_\varepsilon = 0$), thus confining to D_{4h} distortions, a $^5B_{1g}$ ground state in which d_{z^2} is occupied by a single electron is stabilized against the $^5A_{1g}$ ground state with a single occupancy of the $d_{x^2-y^2}$ orbital. The energetic preference of a $^5B_{1g}$ (D_{4h} elongated geometry) against a $^5A_{1g}$ (D_{4h} compressed geometry) ground state is due to the d_{z^2}–4 *s* mixing of the two orbitals of the same a_{1g} symmetry in point group D_{4h}. This electronic effect is missing in the case of a $^5A_{1g}$ ground state and a tetragonal compression, which renders this geometry to become a first-order saddle point (denoted by "*xy*" in the top of Figure 12).

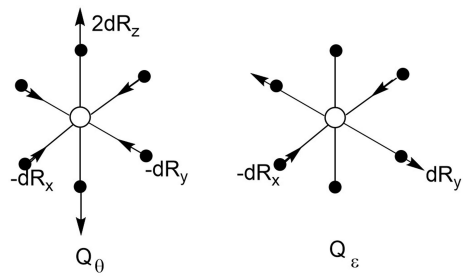

Figure 11. The Jahn-Teller active ε_g vibrations responsible for the vibronic coupling with the ^5E_g ground state of high-spin octahedral $[MnF_6]^{3-}$.

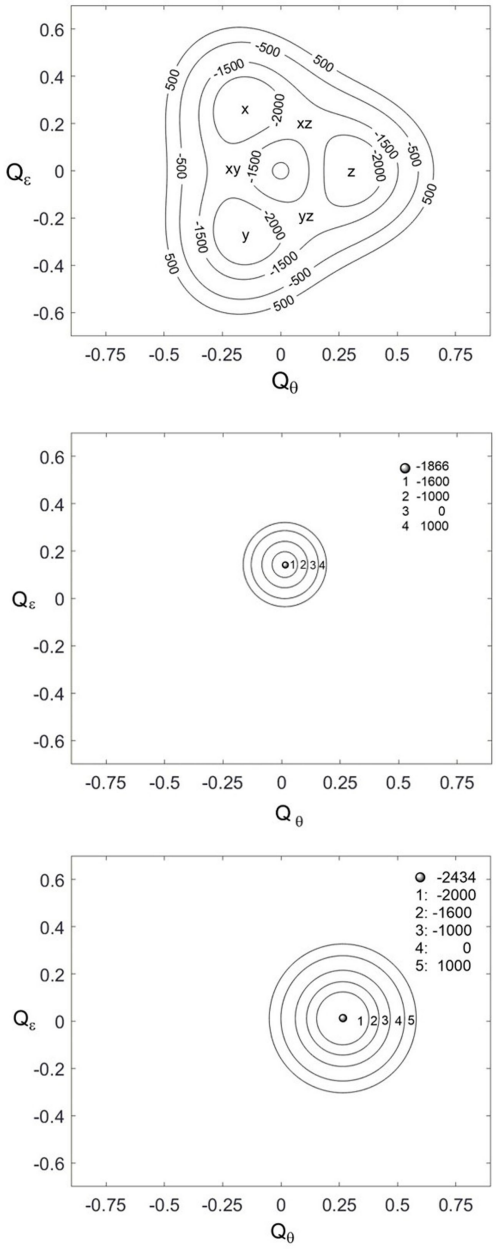

Figure 12. Top: DFT-optimized ground-state potential energy surface of free $[MnF_6]^{3-}$ anions embedded in water. Energy minima, which are stabilized by 2400 cm^{-1} with respect to the regular octahedron for the tetragonally elongated D_{4h} structures with long axes, are shown. The long axes along the *x*, *y* and *z* Cartesian axes are labeled by "*x*", "*y*" and "*z*", respectively. The saddle points between "*x*" and "*z*", "*y*" and "*z*", and "*x*" and "*y*", denoted by "*xz*", "*yz*", and "*xy*", respectively, are stabilized by 1750 cm^{-1} with respect to the regular octahedron. The difference 2400−1750 = 650 cm^{-1} corresponds to the energy barrier between the minima. Middle and bottom: Ground-state potential energy surfaces of the $[MnF_6]^{3-}$ anions in K_3MnF_6, with $[Mn(1)F_6]^{3-}$ (middle) and $[Mn(2)F_6]^{3-}$ (bottom). The potential surfaces were computed by using a vibronic coupling model with parameters adjusted to the reported X-ray structures of $[Mn(1)F_6]^{3-}$ and $[Mn(2)F_6]^{3-}$ and ground-state energy stabilizations for the two sites deduced from NEVPT2 cluster calculations using the X-ray geometries of the two anions, see the Supporting Information for details. Contour level values are in energy units of cm^{-1}.

Table 5. Geometrical parameters [Å] and energies [cm^{-1}] for the stationary points of the ground state adiabatic potential energy surface of the free hydrated $[MnF_6]^{3-}{}_{(aq)}$ anion, in comparison with the pseudo-rhombic $[Mn(1)F_6]^{3-}$ and pseudo-tetragonal $[Mn(2)F_6]^{3-}$ anions in the solid-state compound $K_3[MnF_6]$.

	Free hydrated $[MnF_6]^{3-}{}_{aq}$	Free hydrated $([MnF_6]^{3-})_{aq}$	Solid-state $[Mn(1)F_6]^{3-}$	Solid-state $[Mn(2)F_6]^{3-}$
	Compressed D_{4h}	Elongated D_{4h}	Pseudo-rhombic C_i	Pseudo-tetragonal C_i
$R_x(\Delta R_x)$	2.050(0.065)	1.892(−0.092)	1.856(−0.076)	1.851(−0.082)
$R_y(\Delta R_y)$	2.050(0.065)	1.892(−0.092)	1.999(0.067)	1.863(−0.070)
$R_z(\Delta R_z)$	1.855(−0.13)	2.167(0.183)	1.940(0.008)	2.086(0.153)
R_{av}	1.985	1.984	1.932	1.933
$Q_\theta^o = \sqrt{3}\Delta R_z$	−0.225	0.316	0.014	0.265
$Q_\varepsilon^o = \Delta R_y - \Delta R_x$	0.000	0.000	0.143	0.012
$\lvert A_\theta \rvert$	15300	15300	2530	18300
$\lvert A_\varepsilon \rvert$	15300	15300	25850	800
K_e	58000	58000	180770	69200
$E_{JT}(E_{stab})$	−1750	−2400	(−1866)	(−2434)

Vibronic coupling model for the pseudo-rhombic $[Mn(1)F_6]^{3-}$ and pseudo-tetragonal $[Mn(2)F_6]^{3-}$ sites in K_3MnF_6

In the solid-state compound K_3MnF_6, the $[MnF_6]^{3-}$ complexes undergo two kinds of perturbations. An extrinsic, due to the electrostatic field of the surrounding K^+ ions and an intrinsic, due to vibrations stemming from the ε_g and α_{1g} modes of the (hypothetical) parent octahedron. The electrostatic field due to the lattice ions surrounding each $[MnF_6]^{3-}$ octahedron lowers the symmetry to C_i for both $[Mn(1)F_6]^{3-}$ and $[Mn(2)F_6]^{3-}$ sites. In this symmetry, all three ε_g and α_{1g} become totally symmetric α_g, while the ^5E_g ground term of Mn^{III} splits into two ^5A_g sublevels. The vibronic coupling problem consists of three vibrations coupled to the two ^5A_g states and thus becomes of non-Jahn-Teller type (see the Supporting Information for its mathematical description). Using approximations described in the Supporting Information, this problem simplifies to Equation (3) for the ground state with K_e as the force constant of the two $\alpha_g(e_g)$ vibrations and two linear vibronic coupling constants A_θ and A_ε corresponding to these two (effective) interacting modes.

$$E = (1/2)K_e(Q_\theta^2 + Q_\varepsilon^2) + A_\theta Q_\theta + A_\varepsilon Q_\varepsilon \quad (3)$$

The first term in Equation (3) represents the restoring force which opposes the geometric distortions; the second and the third terms lead to energy stabilizations and thus support the geometric distortions.

In Table 5, we compare K_e, A_θ and A_ε for free hydrated $[MnF_6]^{3-}$ complex anions with their values deduced for the pseudo-rhombic $[Mn(1)F_6]^{3-}$ and the pseudo-tetragonal $[Mn(2)F_6]^{3-}$ anions in the solid state compound K_3MnF_6 (see the Supporting Information how these parameters are obtained for the solid-state).

Upon transition from free, hydrated $[MnF_6]^{3-}$ anions to their solid-state counterparts, the parameters A_θ and A_ε, which by symmetry assume the same values ($A_\theta = A_\varepsilon = A_1$) as in octahedral $[MnF_6]^{3-}$ anions, become essentially different. Thus, A_θ decreases while A_ε increases in magnitude in the case of $[Mn(1)F_6]^{3-}$. These changes reflect *electrostatic perturbations* for the rather ionic lattice of K_3MnF_6 (Figure 3). The large increase of K_e, when going from the free $[MnF_6]^{3-}$ to the $[Mn(1)F_6]^{3-}$ anion in the solid state, reflects the stiffness of the $K_3[MnF_6]$ structure. For $[Mn(2)F_6]^{3-}$ the increase of K_e is smaller compared to $[Mn(1)F_6]^{3-}$ but still exceeds the one for the free $[MnF_6]^{3-}$ anion. When passing from free $[MnF_6]^{3-}$ to the anions in the solid state, the combined effect of the changes of K_e, A_θ, and A_ε leads to distortions for the complexes $[Mn(1)F_6]^{3-}$ and $[Mn(2)F_6]^{3-}$ that are considerably *smaller* than the ones for free $[MnF_6]^{3-}$ anions. This emerges from the values of Q_θ^o and Q_ε^o computed from the deviations of Mn–F bond lengths from the average values of the octahedral $[MnF_6]^{3-}$ complex. The equations relating Q_θ^o and Q_ε^o with ΔR_x, ΔR_y, and ΔR_z are listed in the first column of Table 5. Thus the value of $Q_\theta^o = 0.32$ Å at the energy minimum of the elongated D_{4h} geometry, exceeds the one for $[Mn(2)F_6]^{3-}$ where $Q_\theta^o = 0.26$ Å. We note that the molecular geometry of $[Mn(2)F_6]^{3-}$ is very close to D_{4h}. In contrast to that, the $[Mn(1)F_6]^{3-}$ anion represents a rare case of *an almost entirely rhombically distorted complex*. This is reflected by the very small value of the parameter Q_θ^o and quite significant (but otherwise also small) value of Q_ε^o. In the space of the two effective totally symmetric modes, $[Mn(1)F_6]^{3-}$ distorts exclusively along Q_ε (Figure 11, right). Values of Q_θ^o and Q_ε^o for the $[Mn(1)F_6]^{3-}$ and $[Mn(2)F_6]^{3-}$ anions can be deduced from the crystal structure, while energies for the ground state energy stabilizations are available from NEVPT2 calculations along with Equation (3) (see the Supporting Information for details). Therefore, one can plot the ground state potential surfaces for $[Mn(1)F_6]^{3-}$ and $[Mn(2)F_6]^{3-}$ shown in the middle and at the bottom of Figure 12, respectively.

The comparison between the ground state potential surfaces shown in Figure 12 reflects the break of symmetry when going from the hypothetical free octahedral $[MnF_6]^{3-}$ anion with three equivalent energy minima corresponding to octahedra elongated along the three possible C_4 axes of the octahedron to the particular solid-state $[Mn(1)F_6]^{3-}$ and $[Mn(2)F_6]^{3-}$ anions. This break of symmetry is of extrinsic nature reflecting mainly electrostatic perturbations with main contributions from next-neighbor K^+ ions. Out of the three equivalent minima for the octahedral Jahn-Teller surface, only one, that of the axial elongated $[Mn(2)F_6]^{3-}$ is preserved, however, in a quite modified fashion. While vibronic stabilization energies for the two cases do not differ much (Table 5), the extent of the structural distortions (as reflected by the values of the totally symmetric Q_θ^o and Q_ε^o modes listed in Table 5) is significantly

reduced in the case of $[Mn(2)F_6]^{3-}$. As was stated above and re-emphasized here the $[Mn(1)F_6]^{3-}$ complex is exclusively rhombic in nature.

Conclusions and Outlook

1) $K_3[MnF_6]$ was synthesized by a high-temperature synthesis route and crystallized in a high-temperature/high-pressure approach. The main features of the crystal structure are discrete $[MnF_6]^{3-}$ distorted octahedra that show quite significant geometric distortions. The fourth valence electrons of the d^4-configured Mn^{III} atoms are located in an almost equal mixture of $d_{x^2-y^2}$ and d_{z^2} type MOs in the case of $[Mn(1)F_6]^{3-}$ and in the d_{z^2} orbital of the elongated $[Mn(2)F_6]^{3-}$ anion. According to the single-crystal structure as well as the FTIR spectrum, the substance is free of H_2O and shows no absorption bands of O–H bonds.
2) To the best of our knowledge, the crystal structure of $K_3[MnF_6]$ presents a rare case of two $[MnF_6]^{3-}$ anions with quite different geometries. While the $[Mn(2)F_6]^{3-}$ site represents a pseudo-tetragonal elongated octahedral complex, typical for hexa-coordinate high-spin Mn^{III}, the $[Mn(1)F_6]^{3-}$ anion is a rare example of an almost exclusively Q_ε type rhombically distorted complex. The coexistence of $[Mn(2)F_6]^{3-}$ and $[Mn(1)F_6]^{3-}$ in K_3MnF_6 has been rationalized by using a vibronic coupling model with two totally symmetric normal modes, with parameters adjusted to the X-ray structures of the $[Mn(1)F_6]^{3-}$ and $[Mn(2)F_6]^{3-}$ sites and energy stabilizations deduced from NEVPT2 cluster calculations. Based on this analysis, it is concluded that the stabilization of the pseudo-rhombic complex $[Mn(1)F_6]^{3-}$ originates from a lattice strain effect that largely confines the structures that appear due to the Jahn-Teller effect for free $[MnF_6]^{3-}$ anions. The influence of the lattice on the two $[MnF_6]^{3-}$ anions is manifested by reduced structural distortions compared to a unconstrained free $[MnF_6]^{3-}$ complex, a result due to the lattice stiffness and/or the electrostatic perturbations by nearest-neighbor potassium ions on the Mn^{III} centers.
3) We succeeded in characterizing spectroscopically and magnetically the two different anions in K_3MnF_6. d-d transitions are present in the d-d absorption spectra of both anions. The magnetic anisotropy results from the zero-field splitting of the ^5A_g (C_i point group symmetry) ground states of the pseudo-rhombic $[Mn(1)F_6]^{3-}$ and the pseudo-tetragonal $[Mn(2)F_6]^{3-}$ anions and is reflected in the nesting of the iso-field lines of the magnetizations.
4) Ab-initio cluster calculations show that the rhombic $[Mn(1)F_6]^{3-}$ complex is about 600 cm^{-1} higher in energy than the elongated $[Mn(2)F_6]^{3-}$ complex. With some precaution, it is pointed out that the $K_3[MnF_6]$ reported here might represent a metastable modification of an as-yet unknown compound $K_3[MnF_6]$ with solely tetragonal elongated octahedra, similar to the known $Na_3[MnF_6]$.
5) The presence of two weakly coupled $[Mn(1)F_6]^{3-}$ and $[Mn(2)F_6]^{3-}$ complexes with large magnetic anisotropies allows one to expect magnetostriction, that is lattice deformation and possibly the appearance of different structures upon application of large direct-current magnetic fields and pressures. In the same context, one should also expect slow relaxation of the magnetization in an alternating-current magnetic field. These aspects are of interest for further studies on $K_3[MnF_6]$.

Experimental Section

Synthesis: Single-crystals of $K_3[MnF_6]$ were synthesized in a high-pressure/high-temperature synthetic approach. KHF_2 (Alfa Aesar, Haverhill, USA, 99+ %) and MnO_2 were weight in with a molar ratio of 3:1 and ground together in an agate mortar. Because of the hygroscopic nature of KHF_2, these preparations were conducted under argon inert gas atmosphere employing a glove box (MBraun Inertgas-System GmbH, Germany). The sample was filled in a platinum capsule (99.95 %, Ögussa, Vienna, Austria), inserted into a boron-nitride crucible (Henze Boron Nitride Products AG, Lauben, Germany) and placed in an 18/11 assembly (further details of the assembly are described elsewhere[25–27]). The compression of the assembly was carried out by eight tungsten carbide cubes (Hawedia, Marklkofen, Germany), which were placed in a 1000 t multianvil press (Max Voggenreiter GmbH, Mainleus, Germany) equipped with a Walker-type module (Max Voggenreiter). The sample was compressed to 9.1 GPa within 245 min and kept at this pressure during the heating program. The temperature was raised to 900 °C within 10 min and kept at this temperature for 50 min, followed by cooling of the sample to 550 °C within 90 min. Subsequently, the sample was quenched to room temperature and decompressed within 730 min. The sample was opened in a glove box. It consisted of light pink crystals, which decomposed by contact with ambient conditions (Figure S5, left).

A powder sample of $K_3[MnF_6]$ was synthesized during the PhD thesis of Hofmann in the late 1970ties.[18] MnF_3 and KF were mixed in a ratio of 1:3 and placed in a sealed gold ampoule under argon. This ampoule was stored at 500 °C for 6–10 days. The sample was transferred into a glass ampoule, which was sealed under argon for storage. The ampoule was opened in the year 2019 for measurements that are reported here.

It should be mentioned that it is possible to synthesize this compound by a different high-temperature synthesis route in closed copper ampoules. For this method, KHF_2 and MnO_2 with a ratio of 3:1 were weighed in and ground together under inert gas atmosphere. The mixture was transferred into a copper ampoule and closed in a miniaturized arc-welding equipment.[28] The closed ampule was placed in a silica ampoule, which was evacuated to prevent the copper from oxidation during the heating process. This silica ampoule was placed into a tube furnace and subjected to a temperature of 700 °C for 3 h, followed by quenching of the sample within the oven. The copper ampoule was opened under inert gas atmosphere in a glove box. It was possible to obtain the product $K_3[MnF_6]$ as a dark violet powder (Figure S5, right), but as a side effect of the missing pressure, no single crystals could be isolated.

X-ray structure determination: Powder X-ray diffraction analyses of the high-pressure sample and the one synthesized in copper ampoules were carried out using a Stoe Stadi P powder diffractometer in transmission geometry. $Mo_{K\alpha1}$ ($\lambda = 0.7093$ Å) radiation was used, applying a focusing Ge(111) primary beam monochromator and a Mythen 2 DCS4 detector. The measurement was performed in the 2θ range of 2.0-50.0° with a step size of 0.015°. Figure S6 (top) shows the recorded powder pattern of the high-pressure/high-temperature synthesis plotted against the theoretical powder pattern derived from single-crystal data. Reflections

marked with an asterisk stem from an unknown side product. Figure S6 (bottom) shows the recorded powder pattern of the high-temperature synthesis plotted against the theoretical powder pattern. Reflections belonging to a side phase of K_2MnF_4 are marked with a red asterisk.

The powder X-ray diffraction pattern of the sample synthesized by Hofmann was recorded at ambient temperature with a STOE Stadi MP powder diffractometer in Debye-Scherrer geometry. The diffractometer was operated with $Cu_{K\alpha1}$ radiation (1.5406 Å, Ge(111) monochromator) and equipped with a Mythen1 K detector. The sample was measured in a sealed 0.5 mm glass capillary (Hilgenberg). The evaluation of the powder X-ray patterns was carried out with the WinXPOW 3.07 software package.[29] Rietveld refinement was performed with Jana2006.[30] As starting models, the single-crystal structure reported here and for $KMnF_3$ data from Wang and co-workers, were used.[31]

Light pink single-crystals crystals were isolated under a polarization microscope using perfluoroalkylether for the single-crystal analysis. The intensity data was collected at 183(2) K, as the crystals start to decompose at room temperature under ambient conditions. A Bruker D8 Quest diffractometer (Bruker, Billerica, USA) with $Mo_{K\alpha}$ radiation ($\lambda = 0.7107$ Å), an Incoatec microfocus X-ray tube (Incoatec, Geesthacht, Germany) and a Photon 100 detector were employed. The multi-scan absorption correction of the intensity data was performed with SADABS 2014/5. Based on the extinction conditions, space group $I4_1/a$ (no. 88; Figure S7) was considered for the structure solution (SHELXTL-XT-2014/4) and refinement. The parameter refinement (full-matrix least-squares against F^2) was carried out with SHELXL-2013[32,33] as implemented in the WinGX-2013.3[34] suite. The anisotropic refinement led to values of 0.0295 and 0.0379 for $R1$ and $wR2$ (all data), respectively. Deposition Number 2051984 (for K_3MnF_6) contains the supplementary crystallographic data for this paper. These data are provided free of charge by the joint Cambridge Crystallographic Data Centre and Fachinformationszentrum Karlsruhe Access Structures service Access Structures service.

Vibrational spectroscopy: An FTIR-ATR (attenuated total reflection) characterization of K_3MnF_6 was performed on a Bruker Alpha-P spectrometer (Bruker). The spectrometer was equipped with a 2× 2 mm diamond ATR-crystal and a DTGS detector. The OPUS 7.2 software[35] was used to correct the data set for atmospheric influences.

UV/Vis/NIR spectroscopy: An UV/Vis measurement was carried out on a Varian Cary 5000 UV/Vis/NIR spectrometer with a Praying Mantis accessory (Harrick).

Raman spectroscopy: The Raman spectrum was recorded with a Confocal Raman Microscope S+I MonoVista CRS+, using the 488 nm excitation line of an integrated diode laser (resolution $< 1\ cm^{-1}$).

Magnetic measurements: The magnetic data were recorded using the VSM option of the physical property measurement system (Dynacool, Quantum Design). It was used in the standard VSM setting with a peak amplitude of 2 mm, and a frequency of 40 Hz. Data were collected in the temperature range from 1.8 to 300 K. The magnetic field ranged from −9 to 9 T. The sample was stored in a standard polypropylene sample holder, which was mounted on a brass halfpipe.

Ab-initio and DFT calculations: Calculations were done using the computer package ORCA as documented elsewhere.[36–39] DFT geometry optimizations for the free $[MnF_6]^{3-}$ complexes have been carried out starting from the X-ray molecular geometries of the pseudo-rhombic $[Mn(1)F_6]^{3-}$ and pseudo-tetragonal $[Mn(2)F_6]^{3-}$ units followed by vibrational frequency Hessian calculations at the stationary points of the corresponding molecular geometries. The conductor like polarisable continuum model (CPCM)[40] was used for charge compensation of the excessive negative −3 charge of the complex. In the calculation, the scalar relativistic Douglas-Kroll-Hess (DKH)[41,42] along with the corresponding DKH basis sets were employed. Nonrelativistic correlated CASSCF(NEVPT2) calculations were done using state averaging over all 5 quintet ($S=2$), 45 triplet ($S=1$), and 50 singlet ($S=0$) states spanned by the d^4 configuration of Mn^{III}. To compute the relativistic properties, the magnetizations, magnetic susceptibilities, zero-field tensors, and g-factors, the mean field spin-orbit coupling operator[43] acting within the non-relativistic many-particle basis was used along with quasi degenerate perturbation theory (QDPT).[44] The calculations yield the spectrum of the Hamiltonian and the relativistic spin-orbit wave functions. From these results, the expectation values of the Zeeman-Hamiltonian were evaluated and used to compute the magnetic susceptibilities and isothermal magnetizations. For the calculation of the ZFS tensors and g-factors, we used effective Hamiltonian theory, mapping of the total 210×210 SOC Hamiltonian onto the model space of the lowest magnetic sublevels of ground states $^5A_{1g}$ for the $[Mn(1)F_6]^{3-}$ and $[Mn(2)F_6]^{3-}$ complexes. To facilitate the interpretation of the spectral and magnetic data, the calculations were repeated after reorienting the complexes in a Cartesian frame, in which the ZFS tensor is diagonal (transformation to the canonical axes). All correlated calculations were done using DKH basis sets along with the resolution of the identity and auxiliary basis sets generated automatically by the ORCA code following the method described elsewhere.[45]

Acknowledgements

We thank Sandra Schönegger for the help with the FTIR measurements. Additionally, we thank H. Lars Deubner for measuring Raman spectra, Prof. Dr. B. G. Müller, Giessen, for the long-term storage and donation of the original samples of $K_3[MnF_6]$ synthesized by Dr. Bernhard E. Hofmann working under the guidance of the late Prof. Hoppe. We want to thank Prof. Dr. S. Dehnen for the use of the UV/Vis/NIR device. M.A. and F.N. owe thanks for financial support within the Project "Mangan" of the German Scientific Foundation.

Conflict of Interest

The authors declare no conflict of interest.

Keywords: ab initio calculations · fluorides · single-crystal determination · solid-state reactions

[1] R. Hoppe, W. Liebe, W. Dähne, *Z. Anorg. Allg. Chem.* **1961**, *307*, 276–289.
[2] R. Hoppe, K. Blinne, *Z. Anorg. Allg. Chem.* **1957**, *291*, 269–275.
[3] U. Englich, W. Massa, A. Tressaud, *Acta Crystallogr. Sect. C* **1992**, *48*, 6–8.
[4] G. Siebert. *PhD Thesis*, Justus Liebig-Universität Gießen (Germany), **1972**.
[5] I. G. Ryss, B. S. Wituchnowskaja, *Dokl. Akad. Nauk SSSR* **1954**, *97*, 471–473.
[6] R. D. Peacock, *J. Chem. Soc.* **1957**, 4684–4685.
[7] W. Massa, *Rev. Inorg. Chem.* **1999**, *19*, 118–183.
[8] A. Okazaki, *J. Phys. Soc. Jpn.* **1969**, *26*, 870.
[9] N. Tsukuda, A. Okazaki, *J. Phys. Soc. Jpn.* **1972**, *33*, 1088–1098.

[10] K. A. Pace, V. V. Klepov, T. K. Deason, M. D. Smith, G. B. Ayer, D. P. Diprete, J. W. Amoroso, H. C. Zur Loye, *Chemistry* **2020**, *26*, 12941–12944.
[11] J. Gaˇzo, I. B. Bersuker, J. Garaj, M. Kabešová, J. Kohout, H. Langfelderová, M. Melník, M. Serator, F. Valach, *Coord. Chem. Rev.* **1976**, *19*, 253–297.
[12] N. E. Brese, O'Keeffe, *Acta Crystallogr. Sect. B* **1991**, *47*, 192–197.
[13] I. D. Brown, D. Altermatt, *Acta Crystallogr. Sect. B* **1985**, *41*, 244–247.
[14] R. Hoppe, S. Voigt, H. Glaum, J. Kissel, H. P. Müller, K. Bernet, *J. Less-Common Met.* **1989**, *156*, 105–122.
[15] R. Hoppe, *Angew. Chem. Int. Ed.* **1966**, *5*, 95–106; *Angew. Chem.* **1966**, *78*, 52–63.
[16] R. Hoppe, *Angew. Chem. Int. Ed.* **1970**, *9*, 25–34; *Angew. Chem.* **1970**, *82*, 7–16.
[17] R. Hübenthal *MAPLE, v4*, University of Gießen, Germany, **1993**.
[18] B. E. Hofmann, *PhD Thesis*, Universität Gießen, (Germany), **1979**.
[19] W. E. Hatfield, W. E. Parker, *Inorg. Nucl. Chem. Lett.* **1965**, *1*, 7–9.
[20] D. Reinen, M. Atanasov, W. Massa, *Z. Anorg. Allg. Chem.* **2006**, *632*, 1375–1398.
[21] H. G. Drickamer, *Electronic Transitions and the High Pressure Chemistry and Physics of Solids.* Springer, **1973**.
[22] D. W. Smith, *Struct. Bonding* **1978**, *35*.
[23] K. Nakamoto, *Infrared and Raman Spectra of Inorganic and Coordination Compounds*, Wiley, New York, **1977**.
[24] I. B. Bersuker, *The Jahn-Teller Effect and Vibronic Interactions in Modern Chemistry*, Plenum Press, New York, **1983**.
[25] H. Huppertz, *Z. Kristallogr.* **2004**, *219*, 330–338.
[26] D. Walker, M. A. Carpenter, C. M. Hitch, *Am. Mineral.* **1990**, *75*, 1020–1028.
[27] D. Walker, *Am. Mineral.* **1991**, *76*, 1092–1100.
[28] R. Pöttgen, T. Gulden, A. Simon, *GIT Fachz. Lab.* **1999**, 133–136.
[29] *STOE WinXPOW*, Stoe & Cie GmbH, Darmstadt, Germany, **2015**.
[30] V. Petříček, M. Dušek, L. Palatinus, *Z. Kristallogr. Cryst. Mater.* **2014**, *229*.
[31] S. L. Wang, W. L. Li, G. F. Wang, D. Y. Dong, J. J. Shi, X. Y. Li, P. G. Li, W. H. Tang, *Powder Diffr.* **2013**, *28*, 3–6.
[32] G. M. Sheldrick, *Acta Crystallogr. Sect. A* **2008**, *64*, 112–122.
[33] G. M. Sheldrick, *Acta Crystallogr. Sect. C* **2015**, *71*, 3–8.
[34] L. J. Farrugia, *J. Appl. Crystallogr.* **2012**, *45*, 849–854.
[35] *OPUS, v7.2*, Bruker, Billerica, **2012**.
[36] F. Neese, F. Wennmohs, U. Becker, C. Riplinger, *J. Chem. Phys.* **2020**, *152*, 224108.
[37] F. Wennmohs, F. Neese, ORCA Forum, https:/orcaforum.kofo.mpg.de/app.php/portal.
[38] F. Neese, M. Atanasov, G. Bistoni, D. Maganas, S. F. Ye, *J. Am. Chem. Soc.* **2019**, *141*, 2814.
[39] F. Neese, *Wiley Interdiscip. Rev.: Comput. Mol. Sci.* **2018**, *8*, e1327.
[40] A. V. Marenich, C. J. Cramer, D. G. Truhlar, *J. Phys. Chem. B* **2009**, *113*, 6378–6396.
[41] M. Douglas, N. M. Kroll, *Ann. Phys.* **1974**, *82*, 89–155.
[42] B. A. Hess, *Phys. Rev. A* **1986**, *33*, 3742–3748.
[43] F. Neese, *J. Chem. Phys.* **2005**, *122*, 34107.
[44] D. Ganyushin, F. Neese, *J. Chem. Phys.* **2006**, *125*, 024103.
[45] G. L. Stoychev, A. A. Auer, F. Neese, *J. Theor. Comput. Chem.* **2017**, *13*, 554–562.

Manuscript received: December 28, 2020
Accepted manuscript online: April 8, 2021
Version of record online: May 28, 2021

